ARTICLE NO. 79-4084

Some Observations on the Mechanism of Aircraft Wing Rock

Chintsun Hwang* and W. S. Pi†
Northrop Corporation, Hawthorne, Calif.

A scale model of the Northrop F-5A was tested in NASA Ames Research Center Eleven-Foot Transonic Tunnel to simulate the wing rock oscillations in a transonic maneuver. For this purpose, a flexible model support device was designed and fabricated, which allowed the model to oscillate in roll at the scaled wing rock frequency. Two tunnel entries were performed to acquire the pressure (steady state and fluctuating) and response data when the model was held fixed and when it was excited by flow to oscillate in roll. Based on these data, a limit cycle mechanism was identified, which supplied energy to the aircraft model and caused the Dutch roll type oscillations, commonly called wing rock. The major origin of the fluctuating pressures that contributed to the limit cycle was traced to the wing surface leading edge stall and the subsequent lift recovery. For typical wing rock oscillations, the energy balance between the pressure work input and the energy consumed by the model's aerodynamic and mechanical damping was formulated and numerical data presented.

Nomenclature

A	=	integral of the lift coefficient along the chord, see Eq. (4)
b	=	aircraft wing span
c	=	chord
$\bar{c}$	=	mean aerodynamic chord
c/c_{cr}	=	ratio of mechanical damping constants
c_{cr}	=	critical damping coefficient
C_p	=	pressure coefficient
$C_{\bar{p}}$	=	time-varying static pressure coefficient
C_{l_p}	=	roll damping coefficient
E	=	energy consumed in an oscillation cycle
g_R	=	$2c/c_{cr}$, mechanical damping coefficient
h	=	displacement in plunge
k	=	$\omega\bar{c}/U$, reduced frequency
L_p	=	aerodynamic damping in roll
M	=	Mach number
M_R	=	modal mass in roll
P_i	=	static pressure at station i
Q	=	dynamic pressure
R_N	=	Reynolds number
S	=	wing surface area
U	=	air speed
Wk	=	work done in one oscillation cycle
x	=	chordwise coordinate
y	=	spanwise coordinate
α	=	angle of attack
α^*	=	angle of attack at which wing rock occurs
$\Delta\alpha, \Delta\alpha_s$	=	local angle-of-attack change due to wing rock
β	=	sideslip angle
δ_a	=	aileron settings
δ_h	=	horizontal tail surface setting
δ_n, δ_f	=	leading and trailing edge flap settings
$\varphi, \dot{\varphi}$	=	roll angle and roll rate
ψ	=	yaw angle
ω, ω_R	=	circular frequencies

Received March 1, 1978; revision received Nov. 30, 1978.

Index categories: Handling Qualities, Stability and Control; Transonic Flow; Testing, Flight and Ground.

*Manager, Structural Dynamics Research, Aircraft Group. Associate Fellow AIAA.

†Engineering Specialist, Structural Dynamics Research, Aircraft Group. Member AIAA.

Introduction

IN a transonic maneuver, the combat aircraft has substantial forward speed. In order to place the aircraft in a favorable tactical position, and sometimes to reduce speed, the pilot increases the angle of attack from the normal level flight condition. The increase in angle of attack often occurs simultaneously with a turning and possibly a roll motion. In the initial phase of the maneuver, noticeable vibrations and oscillations appear in the aircraft due to the buildup of the fluctuating pressures. This phase is called buffet onset. As the angle of attack further increases, sustained and large amplitude rigid body oscillations appear, which may be coupled with the flexible vibration modes of the aircraft. The sustained rigid body oscillations, which in varying degree degrade the maneuverability and controllability of the aircraft, are called wing rock. It is known that aircraft wing rock is caused by the lifting surface flow separation. Yet the detailed mechanism of the random and sometimes divergent oscillations of wing rock is not well understood.

In previous investigations on the transonic buffet and wing rock behavior of Northrop F-5A aircraft, the fluctuating pressures and aircraft responses were measured in flight tests. The results and a supplementary analysis were reported in Refs. 1 and 2. Because of the short duration and the transient nature of a transonic maneuver, certain details of the flow mechanism and its resulting fluctuating pressures could be observed only briefly under continuously changing conditions. After evaluating the flight test data, it was felt that a controlled scale model test in a transonic tunnel would shed more light on the wing rock mechanism, if the basic large amplitude oscillations of wing rock could be duplicated. Such a test program was conducted for an F-5A pressure model in the NASA Ames Research Center Eleven-Foot Transonic Wind Tunnel, in two phases. The results of the program are presented in this paper. In the related area of dynamic stall, attention is called to Refs. 3-5.

F-5A Scale Model

A one-seventh scale model of the F-5A aircraft was used in the transonic buffet test program. In the first phase, a nominally rigid sting was used to mount the pressure model. In the second phase, a special sting was designed, incorporating a torsional spring and damper, that allowed the model to oscillate in roll.

Special instrumentation for the model included static and dynamic pressure transducers, accelerometers, and wing root section strain gages. A six component balance was used in the first phase, which was replaced by the flexible support

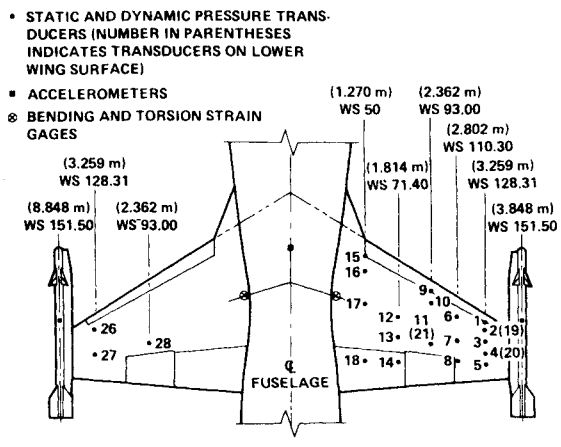

Fig. 1 Dynamic instrumentation of one-seventh scale F-5A pressure model.

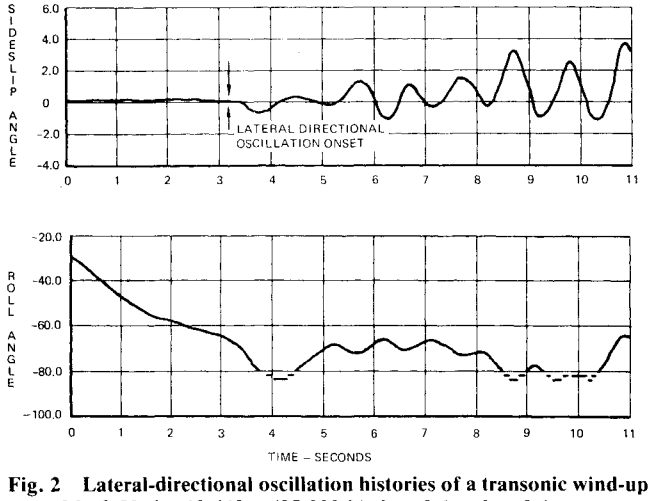

Fig. 2 Lateral-directional oscillation histories of a transonic wind-up turn, $M = 0.89$, $h = 10{,}668$ m (35,000 ft), $\delta_n = 0$ deg, $\delta_f = 0$ deg.

device in the second phase. A drawing showing the dynamic instrumentation locations of the F-5A model is presented in Fig. 1.

The tests were performed encompassing 11 model configurations defined by the external stores and the control surface settings. Three Mach numbers were selected for testing that were nominally identical to those used in the previous flight test program. Other test parameters were the Reynolds number and the nominal sideslip angle. Corresponding to each test condition, various angle of attack settings were used to cover a range up to and above those corresponding to wing rock ($\alpha_{max.} = 16$ deg). In this paper, only selected test cases pertinent to wing rock are presented.

Wing Rock Simulation

Aircraft wing rock appeared during a transonic maneuver when the angle of attack reached a moderate or high amplitude. In the case of the F-5A, depending on the flight condition and aircraft configurations, wing rock appeared at approximately $\alpha = 10$ deg. Wing rock can be described as a Dutch roll type motion, during which the aircraft oscillates in roll, sideslip, and yaw. Typical flight test data of F-5A in which wing rock occurred are shown in Fig. 2, covering the sideslip and roll. Wing rock is related to transonic aileron buzz,[6] in the sense that both phenomena feature unstable oscillations in the transonic region caused by aerodynamic undamping and related to moving shock patterns. In general, the reduced frequency (k) of transonic buzz is at least one order of magnitude higher than that of wing rock.

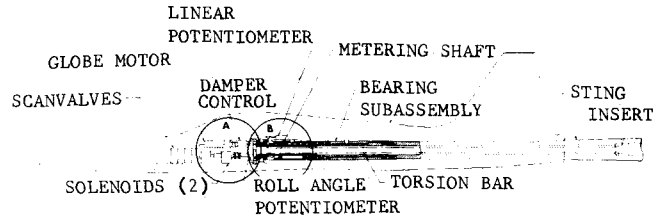

Fig. 3 Section view of the F-5A scale model and the flexible roll device mounted on the sting.

In a wind tunnel test program, it was not possible to simulate all the oscillating degrees of freedom of wing rock, especially under severe dynamic pressure conditions. The subject test program was conducted with a flexible support featuring a lightly damped roll degree of freedom. The model and the flexible support were installed at the end of a specially designed sting. The flexibility of the sting allowed the model to oscillate slightly in yaw, sideslip and pitch during the simulated wing rock oscillations. It will be shown in a later section of this paper that the roll oscillation, interacting with the angle of attack and the sideslip angle, was the major contributing factor to local flow separation, which in turn caused wing rock.

The Flexible Support System

The full-scale F-5A displayed a wing rock natural frequency of about 0.5 to 1.0 Hz. This corresponded to a model frequency of 3.5 to 7.0 Hz. Since it was neither practical nor desirable to allow the model to rotate freely about the roll axis in a wind tunnel test, a support system with a flexible roll constraint was designed for phase II of the test program. This roll constraint had a natural frequency approximately equal to the natural wing rock frequency , so that the impedance corresponding to the desired roll mode was minimized. The system allowed the model to oscillate ± 30 deg in roll. An adjustable damping device and a roll angle measuring potentiometer also formed part of the assembly. Except for the elimination of the balance unit, the pressure and response data instrumentations of the model remained unchanged from the first tunnel entry (phase I). Dynamic data such as the roll angle, the model pitch and yaw oscillation angles, and the damping coefficients of the damper were recorded.

The flexible support unit (see Fig. 3) was assembled with a specially designed hollow sting whose external dimensions were identical to the standard sting used in the Eleven-Foot Transonic Tunnel. A torsion bar was installed inside the sting. The rear end of the bar was anchored to the sting at a location approximately ⅓ the length from the front of the sting. The torsion bar was designed to oscillate with the scale model along the roll axis with a natural frequency of 3.5 Hz in still air. The front portion of the sting was machined to accept two needle bearings and two lightweight thrust bearings, which were fitted into the inside of a sleeve-shaped spacer. After the bearings were assembled, the spacer was rigidly tied to the model fuselage body.

Beyond the bearing subassembly, the front tip of the sting was fitted with internal splines. The splines were used to accept the rear end of the damper subassembly shaft. The damper subassembly (see Figs. 3 and 4) consisted essentially of the internal shaft and the external housing, and their attachments. The internal shaft was tied through the external splines to the sting front end. It was thus stationary along the roll axis. The external housing was tied to the scale model through locating pins. The damper shaft was assembled with a 240-deg partial cylinder to form a 120-deg fan-shaped cavity on top of the shaft. Correspondingly, the damper housing was attached with a fan-shaped piston, which covered an arc of 60 deg. When properly assembled with a number of seals and spacers, etc., and hydraulic liquid added to the cavity, the

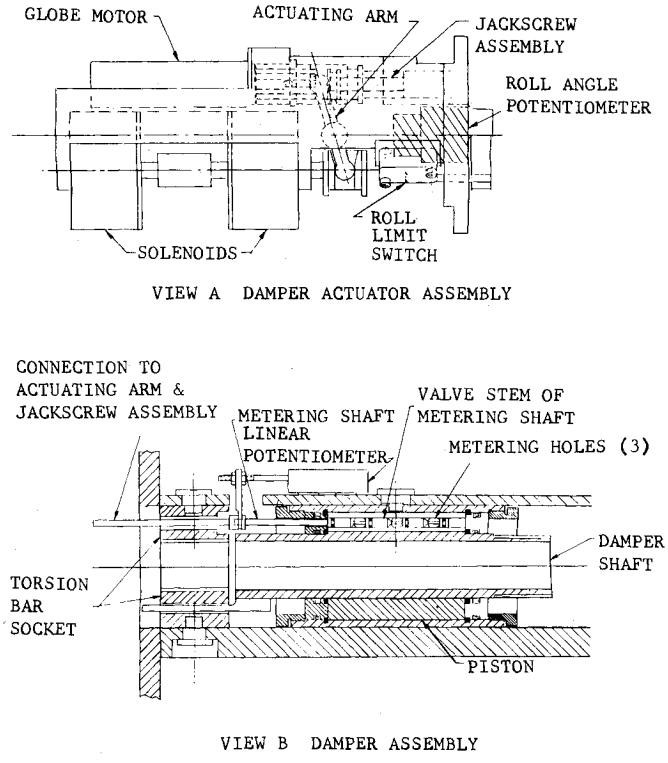

Fig. 4 Details of the flexible roll device actuator and damper assemblies.

damper housing could rotate ±30 deg about the shaft subassembly, while the hydraulic liquid was forced to move from one side of the piston to the other through three metering holes cut in the piston (see Fig. 4, View B). The sizes of the metering holes, which allowed the liquid to move, were controlled by a spool shaft. By adjusting the lengthwise position of the spool shaft, the metering holes were left either completely open, partially open, or completely blocked. In this manner, the amount of damping supplied by the damper was controllable. The damper unit was locked out and the model prevented from roll oscillation when the metering holes were completely blocked by the spool shaft. The linear movement of the spool shaft was controlled by a motor-operated jackscrew device (see Fig. 4, View A). To prevent model damage in an emergency, the fast-acting lockout mechanism of the spool shaft was activated by two solenoids. In front of the damper unit, and behind the two solenoids inside the model fuselage, an angular potentiometer was used to measure the roll angle of the scale model relative to the sting.

Prior to the presentation of the test data, it was necessary to establish the relation between the roll and yaw oscillations and the local angle-of-attack changes. Ignoring the less significant terms, the local $\Delta\alpha$ change at a semispan location of the wing was

$$\Delta\alpha = -\varphi\cos\alpha\tan\beta + (\dot{\varphi}y/U)\frac{\cos\alpha}{\cos\beta} - \psi\sin\alpha\tan\beta \qquad (1)$$

where φ was the roll angle measured from the mean position. In the wing rock motions observed during flight tests, the yaw oscillation amplitude was always smaller than the corresponding roll oscillation. Since the critical α angle was in the range of 10 deg to 16 deg, the contribution of ψ to $\Delta\alpha$, as represented by the last term of Eq. (1), was substantially less than the term involving the roll angle φ. In other words, the first two terms on the right side of Eq. (1) were the main contributing factors to $\Delta\alpha$, which was known to be the cause

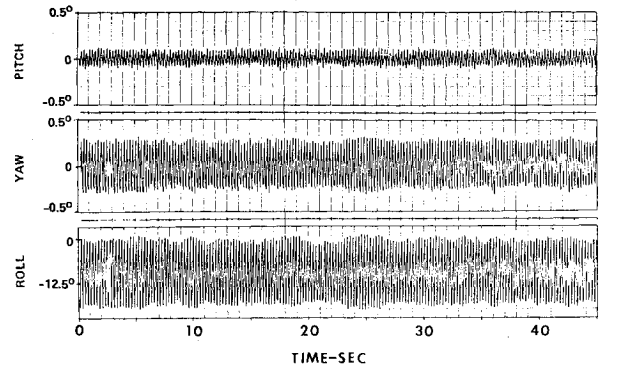

Fig. 5 Time histories of F-5A model pitch angle, yaw angle and roll angle recorded during run 26, phase II, $\alpha = 10$ deg, $\beta = 8$ deg, $M = 0.925$, $\delta_n/\delta_f = 0/0$ deg, $\delta_h = -10$ deg.

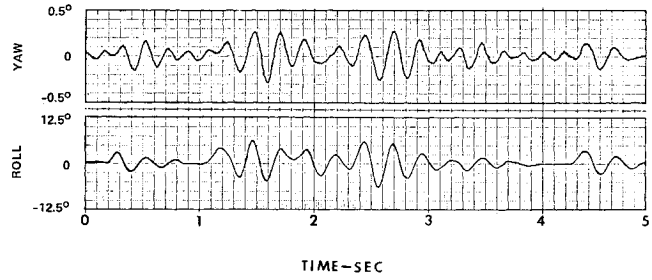

Fig. 6 Time histories of F-5A model yaw angle and roll angle recorded during run 5, phase II, $\alpha = 10$ deg, $\beta = 0$ deg, $M = 0.925$, $\delta_n/\delta_f = 5/12$ deg, $\delta_h = 0$ deg.

of wing rock. The above observation served to justify the use of a flexible roll device to approximately simulate wing rock oscillations.

Aerodynamic Hysteresis and the Limit Cycle Concept

In phase II, two types of model oscillations along the roll axis were observed. In one type, the oscillation was approximately a constant-amplitude sinusoidal motion. The corresponding local pressure data also featured a periodic pattern, even though highly nonlinear with respect to the model motion. In a second type, the oscillation was essentially sinusoidal with the amplitude of the oscillation changing from cycle to cycle. The roll motion exhibited a pattern of irregular bursts, interspersed by periods of near-zero oscillation. The first type of oscillation was named the stationary type; a typical case was run 26, phase II (Fig. 5) with the following test conditions:

$$\delta_n/\delta_f = 0/0 \text{ deg}, \delta_h = -10 \text{ deg}, \delta_a = 0/0 \text{ deg}$$

$$M = 0.925, Q = 17.95 \text{ kN/m}^2 (375.0 \text{ psf})$$

$$R_N = 7.382 \times 10^6/\text{m} (2.25 \times 10^6/\text{ft}), \text{ or } 2.48 \times 10^6$$

based on the mean aerodynamic chord of the model,

$$\alpha = \alpha^* = 10 \text{ deg}, \beta = 8 \text{ deg}, c/c_{cr} = 0.012$$

The corresponding run in phase I is run 51, which had the identical model configuration and test Reynolds number as run 26, phase II, just shown. The phase I runs were made with a standard sting with minimum roll flexibility, whereas in phase II, a special sting with substantial roll flexibility was used.

The second type of oscillation was named the nonstationary type. A typical case was run 5, phase II (Fig. 6), with the test

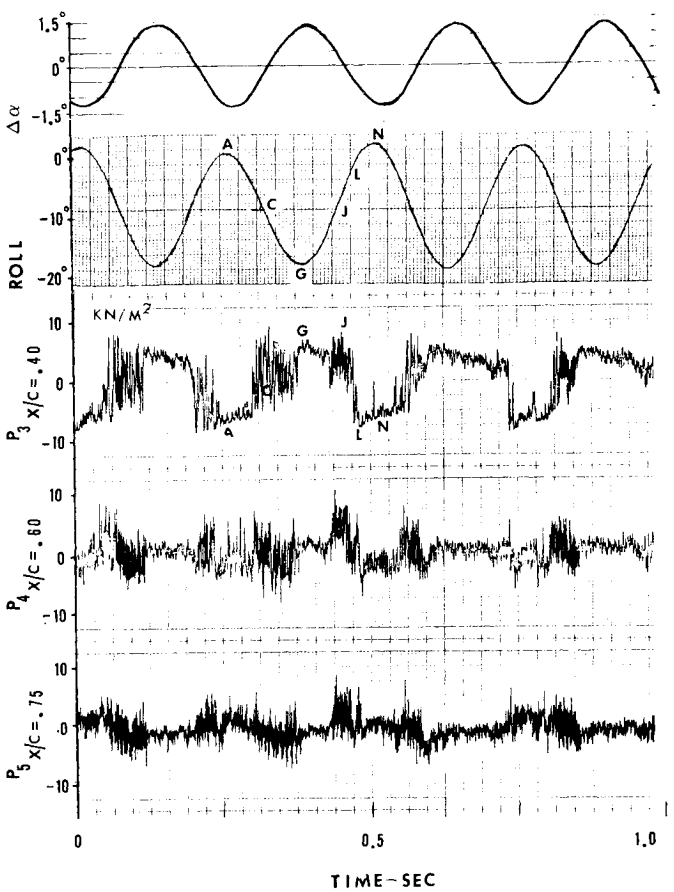

Fig. 7 Real-time data of the roll oscillations and the corresponding local pressures of transducers numbers 3, 4, 5 of the F-5A scale model, run 26, phase II, $\alpha = 10$ deg, $\beta = 8$ deg, $M = 0.925$, $\delta_n/\delta_f = 0/0$ deg, $\delta_h = -10$ deg, $Q = 17.95$ kN/m^2, $c/c_{cr} = 0.012$.

conditions as shown below:

$$\delta_n/\delta_f = 5/12 \text{ deg}, \delta_h = 0 \text{ deg}, \delta_a = 0/0 \text{ deg}$$

$$M = 0.925, Q = 18.20 \text{ kN/m}^2 (377.7 \text{ psf})$$

$$R_N = 7.382 \times 10^6/\text{m} (2.25 \times 10^6/\text{ft}), \text{ or } 2.48 \times 10^6$$

based on the mean aerodynamic chord of the model,

$$\alpha = \alpha^* = 10 \text{ deg}, \beta = 0 \text{ deg}, c/c_{cr} = 0.057$$

The corresponding phase I data are from run 8, with identical test Reynolds number.

The real-time roll oscillation and the corresponding fluctuating pressure data are illustrated in Fig. 7, for run 26, phase II. In the figure, P_3, P_4, P_5 represent the local fluctuating pressures at 85% semispan of the right wing top surface, with transducers located at 40%, 60%, and 75% chordwise positions. On top of the oscillograph plots, the local $\Delta\alpha$ oscillation was presented, based on Eq. (1) with the third term on the right side omitted. In examining the fluctuating pressure data versus the local $\Delta\alpha$ changes, it was apparent that the sudden pressure changes, representing the loss of lift or lift recovery, and the high amplitude oscillations, representing the unstable shock movement during transition from local unseparated flow to flow separation (or vice versa), followed a cyclic pattern. This cyclic pattern was synchronized with the local $\Delta\alpha$ changes. Specifically, when the local $\Delta\alpha$ was changed from negative to positive, the shock oscillations and the subsequent flow separation tended to lead the $\Delta\alpha$ change. When the $\Delta\alpha$ was changed from positive to negative, the local pressure change (a lift recovery) was usually more clear cut, reflecting the momentum of the local flow moving the shock front rearward toward the trailing edge. It was also noted that the model roll oscillation frequency was 3.9 Hz, substantially higher than the still air natural frequency of 3.5 Hz. The detailed behavior of the fluctuating pressures and their impact on aircraft wing rock can best be studied together with the static pressure development on the wing surfaces.

In Figs. 8 and 9, the chordwise static pressure distributions‡ for run 51, phase I and run 26, phase II are plotted side by side to illustrate the effect of roll oscillations to local static pressure distributions. Both figures are for 85% semispan of the right wing. Figure 8 shows the upper surface pressure data corresponding to the nominal angle of attack range from 0 deg to 12 deg. Figure 9 shows the lower surface static pressure data for selected α's when substantial changes in upper surface pressures took place.

Referring to Fig. 8, for phase I corresponding to a standard rigid sting, the high pressure gradient near the midchord for $\alpha = 6$ deg to 8 deg indicated a shock-induced flow separation in the near semichord region. At $\alpha = 10$ deg, the shock moved forward and became less distinct. As a result, the pressure gradient was more evenly distributed along the chordwise location. With the angle of attack at $\alpha = 12$ deg, a major breakdown of the unseparated flow occurred. At this α, the leading edge induced flow separation caused a substantial loss in lift in the outer semispan of the wing. (The onset of flow breakdown appeared at α slightly greater than 10 deg.)

The phase II data of Fig. 8 shows the corresponding static pressure distribution at 85% semispan when the model was free to oscillate along the roll axis. The test results indicated the model was nearly stationary up to $\alpha = 9.6$ deg. As expected, the static pressure data up to this α closely resembled the phase I data. At $\alpha = \alpha^* = 10.3$ deg, sustained roll oscillation took place with a roll frequency of 3.9 Hz. Selected real-time response and fluctuating pressure data at this α were shown previously in Fig. 7. The ranges LG, $L'G'$, in Fig. 8, indicated the extent of the fluctuating pressure changes based on Fig. 7 data. Beyond $\alpha = 10.3$ deg, the roll oscillations either had reduced amplitude, or in some cases, completely disappeared. Correspondingly, the static pressure distribution at 85% semispan followed a similar pattern to that acquired in phase I.

The lower surface static pressure data—corresponding to the critical α range when drastic pressure redistribution took place on the upper surface of the right wing— are plotted for both phases in Fig. 9. In examining these data, and the real-time fluctuating pressure data of the lower surface, it can be concluded that the lower surface flow was not affected to any appreciable degree by the model oscillation. In other words, little or no interaction between the lower surface pressure distribution and the aircraft oscillatory movements was observed.

In order to investigate the static and dynamic pressure behavior on the left wing (the leeward side for $\beta = 8$ deg) corresponding to the same test condition (run 26, phase II) when sustained roll oscillations took place, the data of run 27, phase II, for the right wing, were examined (Fig. 10). Run 27 was performed with the identical model and tunnel conditions of run 26, except that $\beta = -8$ deg. The use of the leeward side (right) wing pressure data of $\beta = -8$ deg to replace the leeward side (left) wing pressure data of $\beta = 8$ deg was necessary because of the scant number of pressure transducers installed on the left wing. The above substitution implied the

‡The static pressure data of phase I is the steady-state data. For phase II, because of the time-varying nature of the pressure data caused by the wing rock motion, the static pressure is the time average of the so-called steady-state data.

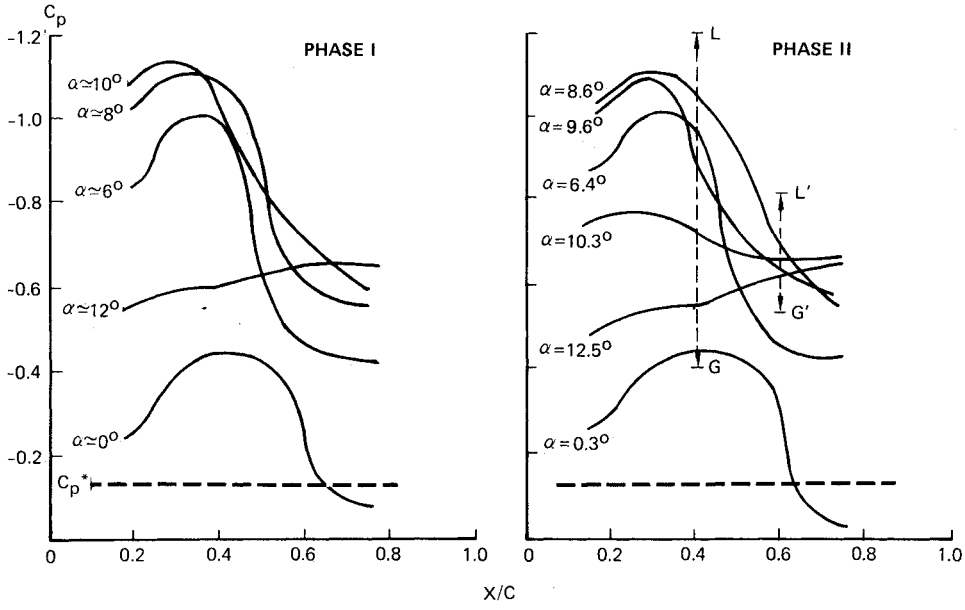

Fig 8 Chordwise static pressure distribution at the top surface of 85% semispan, F-5A right wing: The left plot based on run 51, phase I data; the right plot based on run 26, phase II mean value data; LG, $L'G'$ indicate range of fluctuating pressures for $\alpha_{nominal} = 10.3$ deg.

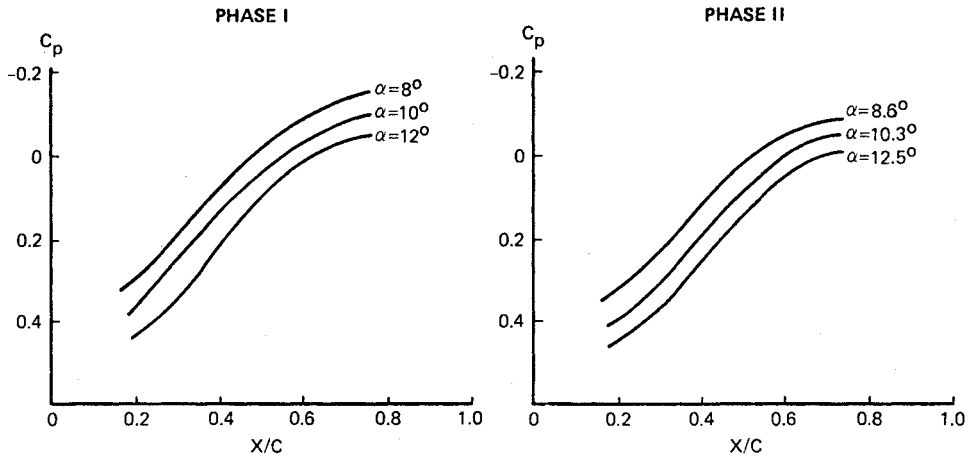

Fig. 9 Chordwise static pressure distribution at the bottom surface of 85% semispan, F-5A right wing: The left plot based on run 51, phase I data; the right plot based on run 26, phase II mean value data.

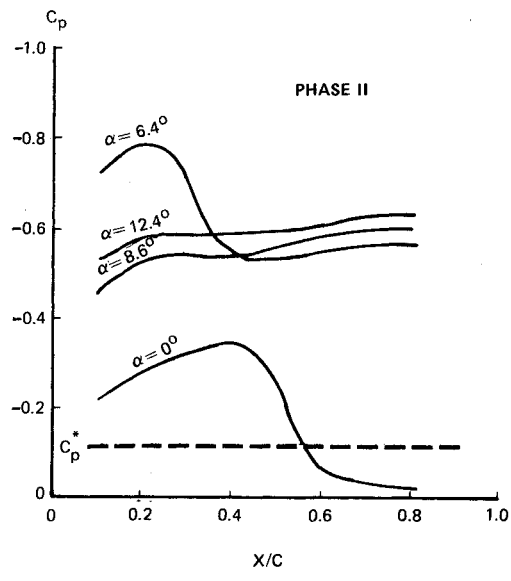

Fig. 10 Chordwise static pressure distribution at top surface of 85% semispan, F-5A right wing, based on run 27, phase II, mean value data, $Q = 17.95$ kN/m^2.

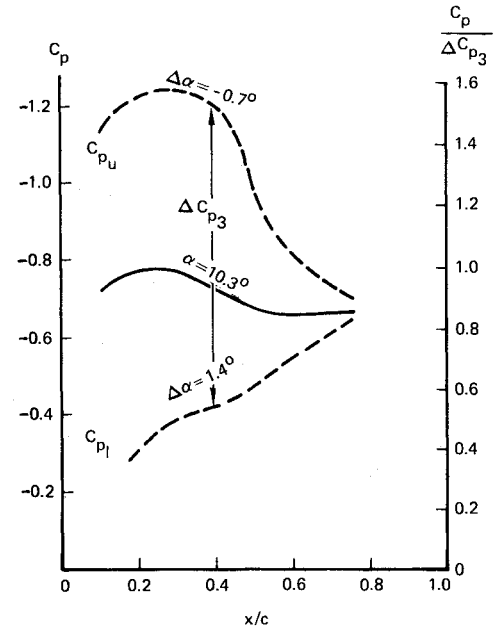

Fig. 11 Range of spanwise static pressure distribution at top surface of 85% semispan, F-5A right wing during simulated wing rock oscillations, run 26, phase II, $Q = 17.95$ kN/m^2.

assumption of perfect symmetry of the test model and the wind tunnel along their central sections.

Referring to Fig. 10, and comparing the data with windward side data of Fig. 8, it was seen that prior to complete flow separation, the lift distribution on the leeward side was lower than that on the windward side. This behavior was partially attributed to the positive sideslip angle of run 26, which acted with the wing sweepback to reduce the mean effective angle of attack on the leeward (left) side. At higher α, the vortex shedding and wake turbulence effect of the fuselage, and possibly other factors, contributed to the asymmetrical pressure distribution of the wing. In general, complete flow separation appeared earlier on the leeward wing in the upper surface near the wingtip. It was also noted that the static pressure on the leeward wing surface varied in a moderate manner during the roll oscillations at the critical angle of attack, $\alpha^* = 10.3$ deg. Available information indicated that with sideslip, the major contributing factor to wing rock of the F-5A was due to the pressure fluctuation on the top surface of the windward semispan.

Combining the mean static pressure data of Fig. 8 corresponding to $\alpha = 10.3$ deg for run 26, phase II, and the extreme fluctuating pressure data taken from points such as *G, L,* identified in Fig. 7, a plot of the range of the chordwise pressure distribution during a roll oscillation cycle is shown in Fig. 11.

An examination of Fig. 11 indicated dynamic overshoot of the static pressures for both positive and negative $\Delta\alpha$. For negative $\Delta\alpha$, the maximum lift was generated along the chord section higher than the lift recorded in steady state tests. The maximum lift occurred prior to the time when the minimum $\Delta\alpha$ value was reached, indicating a phase lead of 30 deg to 45 deg. Using the convention of Ref. 3 for α overshoot, the following may be stated for the wing strip in the neighborhood of 85% semispan:

$$\Delta\alpha_s = K_a\left[-\varphi\cos\alpha\tan\beta + (\dot{\varphi}y/U)\frac{\cos\alpha}{\cos\beta}\right] \qquad (2)$$

$K_a \cong 2$ where K_a is the dynamic overshoot coefficient. The

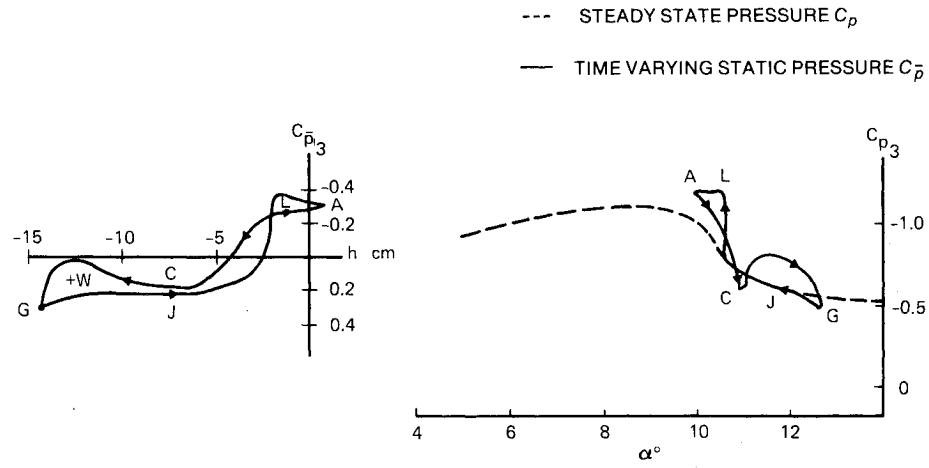

Fig. 12 Steady state pressure coefficient C_p and time varying pressure coefficient $C_{\bar{p}}$ vs local translatory motion h and local angle of attack α, as observed from the oscillating model of F-5A, pressure transducer no. 3, run 26, phase II, $\beta = 8$ deg, $M = 0.925$, $\beta = 8$ deg, $M = 0.925$, $\delta_n/\delta_f = 0/0$ deg, $\delta_h = -10$ deg, $Q = 17.95$ kN/m^2, $c/c_{cr} = 0.012$.

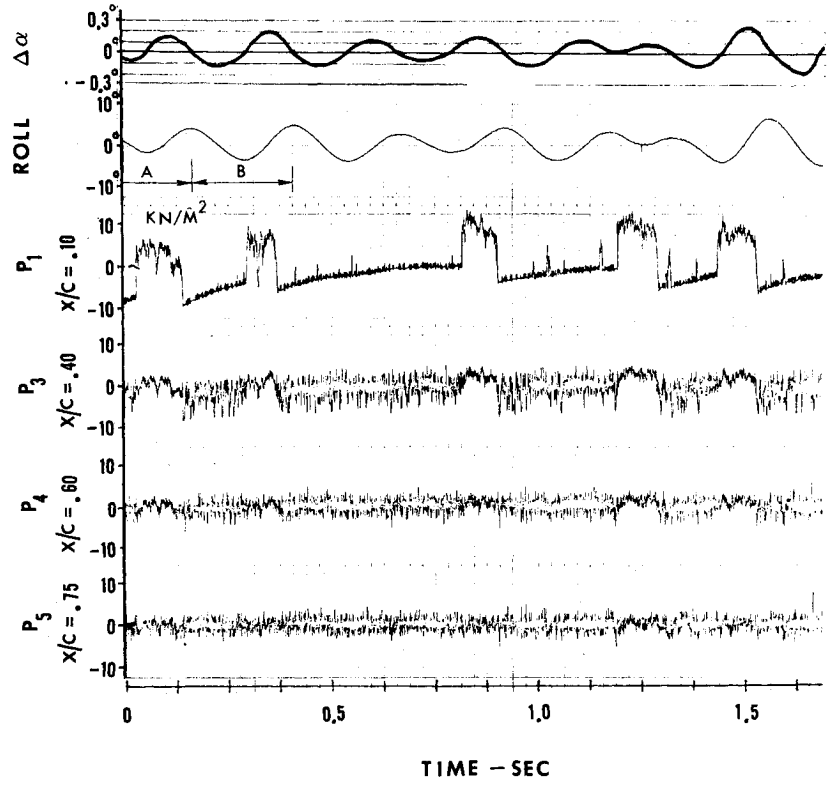

Fig. 13 Real-time data of the roll oscillations and the corresponding local pressures of transducer numbers 1, 3, 4, 5 of the F-5A scale model, run 5, phase II, $\alpha = 10$ deg, $\beta = 0$ deg, $M = 0.925$, $\delta_n/\delta_f = 5/12$ deg, $\delta_h = 0$ deg, $Q = 18.2$ kN/m^2, $c/c_{cr} = 0.057$.

above equation and the pressure data, as illustrated in Figs. 7-11, indicated that the oscillating dynamic loads, if any, were dependent on the amplitude and phase of the roll oscillations during wing rock. The dynamic loads and the motion thus formed an interacting pair. The existence of limit cycle-type oscillations was determined by the energy balance of the input to the aircraft in the form of fluctuating loads caused by motion-induced flow separation, and the energy consumed by aerodynamic damping when the aircraft oscillated in roll, possibly with other coupled motions. The energy input to the aircraft, essentially due to the fluctuating pressure loads on the top surface of the right wing for $\beta = 8$ deg, may be computed based on the C_p data versus the local translatory motion due to the roll oscillation. In Fig. 12, the local C_p data for a typical station P_3 are plotted versus the translatory motion h and the local angle of attack $\alpha + \Delta\alpha$. To estimate the work done by the fluctuating forces in one oscillation cycle, the following assumptions are made:

1) The work was essentially in the form of the fluctuating pressure applied to the top surface of the windward semispan, and may be represented by the loads on a wing strip with width Δb, located at 85% semispan. The corresponding local oscillatory motion is $he^{i\omega t} = \varphi y e^{i\omega t}$.

2) The C_p contour along the chordwise direction was defined by the upper and lower limit values of Fig. 11. The fluctuating pressures varied in coordination with each other so that the limit cycle loop described in Fig. 12 for C_{p_3} was followed by all pressures along the chordwise direction.

Applying the preceding assumptions, the work input per oscillation cycle simulating wing rock is

$$Wk = \oint C_{p_3} \Delta b A Q \mathrm{d}h \tag{3}$$

$$A = \int_0^c \frac{C_{p_l} - C_{p_u}}{\Delta C_{p_3}} \mathrm{d}x \tag{4}$$

where C_{p_l}, C_{p_u} are the lower and upper C_p values defined in Fig. 11. A is the area covered by C_{p_l} and C_{p_u} and is integrated from the leading edge to the trailing edge, using the scale on the right hand of the plot. The integral $\oint$ covers the complete oscillation cycle.

In the following paragraphs, the energy consumed by damping is considered. The aerodynamic damping in roll, as represented by the coefficient C_{l_p}, is applied in the limited sense that it covers only the roll damping when no flow separation and lifting surface stall take place. It is used to account for the energy balance including the limit cycle mechanism, as shown in Fig. 12. When the net energy transfer is considered, there exist cases where the aerodynamically originated energy input to the aircraft per cycle of oscillation is positive. For those cases, the overall roll damping is negative, i.e., aerodynamic undamping.

Applying the above convention, the energy consumed by aerodynamic damping in roll and the mechanical damping built into the model support system is

$$E = \oint (g_R M_R \omega_R - L_p) \dot{\varphi} \mathrm{d}\varphi \tag{5a}$$

$$L_p = C_{l_p} QSb^2/2U \tag{5b}$$

The energy balance condition for constant amplitude wing rock oscillation is then

$$\oint C_{p_3} \Delta b A Q \mathrm{d}h = \oint (g_R M_R \omega_R - L_p) \dot{\varphi} \mathrm{d}\varphi \tag{6}$$

In the above equation, the value Δb, or the effective width of the wingtip area with significant fluctuating pressures to supply work to the limit cycle, is treated as a parameter. This parameter is determined by the energy balance condition. The numerical values of the parameters used to calculate the energy balance condition of the F-5A model for run 26, phase II, $\alpha = \alpha^* = 10$ deg are the following:

M_R	$= 0.00437\ \mathrm{m^2 - kg}$	g_R	$= 2c/c_{cr} = 0.024$
ω_R	$= 25.13$ rad/s	Q	$= 17.95\ \mathrm{kN/m^2}$
S	$= 0.3244\ \mathrm{m^2}$	b	$= 1.1$ m
U	$= 299$ m/s	c_{l_p}	$= -0.135$
A	$= 0.1076$ m	$\oint C_{p_3} \mathrm{d}h$	$= 0.0163$ m
$\varphi_{\max.}$	$= 9$ deg	$\oint \dot{\varphi} \mathrm{d}\varphi$	$= \pi \varphi_{\max.}^2 \omega_R = 2.17\ s^{-1}$

Based on the preceding data, an estimate of energy balance was reached as follows:

$$E = 6.159 \text{ m-N/cycle}$$

of which 43.5% was due to mechanical damping, 56.5% due to aerodynamic damping.

$$Wk = 0.3445 \Delta b \text{ m-N/cycle}$$

$$\Delta b = 0.35\,(b/2) = 0.1923 \text{ m}$$

The real-time roll oscillations and the fluctuating pressure data of run 5, phase II are illustrated in Fig. 13. The approximate $\Delta\alpha$ data due to the local downwash and upwash strokes were generated and plotted on the top of the figure. P_1, P_3, P_4, and P_5 were located at 85% semispan right wing top surface, and at 10, 40, 60, and 75% chordwise positions,

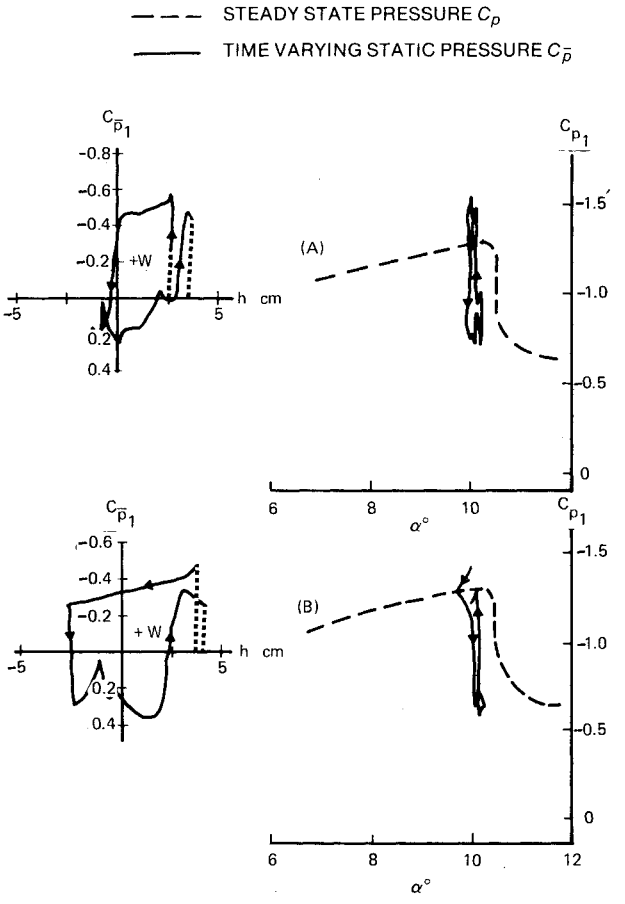

Fig. 14 Steady state pressure coefficient C_p and time varying static pressure coefficient $C_{\bar{p}}$ vs local translatory motion h and local angle of attack α, as observed from the oscillating model of F-5A, pressure transducer no. 1, run 5, phase II, $\beta = 0$ deg, $M = 0.925$, $\delta_n/\delta_f = 5/12$ deg, $\delta_h = 0$ deg, $Q = 18.2\ \mathrm{kN/m^2}$, $c/c_{cr} = 0.057$.

respectively. Run 5 was conducted with zero β. The roll oscillation amplitude was substantially lower than the corresponding value of run 26, phase II (see Fig. 7), partially because of the higher mechanical damping, g_R, of the support system. The oscillations were irregular and intermittent.

In examining Fig. 13 data, it was noted that the flow at P_1 was unseparated for the majority of the time, with intermittent lift losses, which were synchronized with $\Delta\alpha$ changes. The continuous pressure fluctuations at P_3, P_4, and P_5 indicated a separate flow, induced by a shock located somewhere between 10 and 40% chordwise positions. The lift losses at P_1 (i.e., sudden pressure increases) appeared when $\Delta\alpha \simeq 0$ and $\dot{\alpha} = +$, a condition inducing leading edge stall and local flow separation. The lift losses at $\Delta\alpha \simeq 0$ indicated a phase lead of the flow separation caused by the dynamic effect. The lift recovery at P_1 appeared at $\dot{\alpha} = -$, even though $\Delta\alpha$ was still positive at the time. The overall picture was a state of moderate instability, with the shock line located close to the leading edge. An intermittent movement of the shock line toward the leading edge caused the complete stall of the local section. The local stall was partially recovered within ½ oscillation cycle or less. Typical limit cycle area for P_1 are presented in Fig. 14. In the figure, the local C_{p_1} vs α data were also plotted. The very limited $\Delta\alpha$ changes kept the C_p variation away from the ramp corresponding to the steady state loss of lift. The narrow $\Delta\alpha$ range for the test case was considered restrictive, not being a typical free-flight condition.

It was also noted in Fig. 14 that, if the random turbulences were ignored, the cyclic pressure fluctuations (being the source of the limit cycle energy input) appeared only near the outer span leading edge area. This was in contrast to the run 26, phase II case, where the pressure fluctuations appeared in substantial amplitude throughout the majority of the chord length (see Fig. 7). As a result, the wing rock type oscillations of run 5, phase II, representative of cases of zero β, were intermittent and limited in oscillation amplitude.

The energy-balanced condition for each cycle of nonstationary wing rock oscillation, such as cycle A or B of Fig. 13 is

$$Wk = \tfrac{1}{2} M_R \omega_R^2 (\varphi_2^2 - \varphi_1^2) + \oint (g_R M_R \omega_R - L_p) \dot{\varphi} \mathrm{d}\varphi \qquad (7)$$

where φ_1, φ_2 are the initial and terminating roll oscillation amplitudes (at $\dot{\varphi} = 0$) of the oscillation cycle. The first term in the right-hand side of the above equation denotes the potential energy change of the flexible roll device. Assumptions made for the work were similar to those made in the stationary ($\beta \neq 0$) case, except that, for $\beta = 0$, top surface strips Δb on both sides of the wing contributed to the limit cycle. The following numerical data were applied for a typical oscillation cycle (cycle B in Figs. 13 and 14):

g_R	$=0.114$	Q	$=18.2$ kN/m^2
U	$=301.1$ m/s	A	$=0.0524$ m
$\oint C_{p_1} \mathrm{d}h$	$=0.00308$ m	φ_1	$=4$ deg
φ_2	$=5$ deg	$\oint \dot{\varphi} \mathrm{d}\varphi$	$=0.3767$ s^{-1}
E	$=2.82$ m-N/cycle		

of which 76.6% was due to mechanical damping, 21.4% to aerodynamic damping.

$$Wk = 2 \oint C_{p_1} \Delta b A Q \mathrm{d}h = 5.88 \Delta b \text{ m-N/cycle}$$

$$PE = \tfrac{1}{2} M_R \omega_R^2 (\varphi_2^2 - \varphi_1^2) = 1.776 \text{ m-N/cycle}$$

$$\Delta b = 0.1425(b/2) = 0.077 \text{ m}$$

As described previously, the cyclic fluctuation pressure that contributed to the bulk of the limit cycle work input (with or without sideslip) appeared near the outer span leading edge area of the wing top surface. Based on the above results, the effective wing strip width Δb, for the case with zero β, was 14.25% of the semispan, as against 35% of the semispan for the sideslip case. The difference in the Δb values for the two cases highlighted the strong contribution of the sideslip to aircraft wing rock.

Conclusions

In evaluating the preceding data representing the stationary and the nonstationary cases simulating wing rock, the following conclusions were drawn:

1) Wing rock was generated by a limit cycle mechanism due to the fluctuating pressure changes on the wing top surface, especially near the wing tip region. In the cases observed, the major reason for the pressure changes was the motion induced $\Delta\alpha$, which alternatively caused leading edge stall and recovery. The amount of energy input to the limit cycle, to be consumed by aerodynamic and/or mechanical damping, may be evaluated quantitatively.

2) Based on kinematics, the roll oscillations acted together with α and β, to cause substantial $\Delta\alpha$ changes, which contributed to the limit cycle. Wing rock amplitude was thus dependent on the steady-state sideslip angle β. To a minor degree, the yaw oscillation also contributed to wing rock limit cycle.

3) With a sideslip angle β, the upper wing surface on the windward side contributed the majority of the fluctuating pressures that caused wing rock.

4) With $\Delta\alpha$, the local fluctuating pressure coefficient followed the ramp curve during leading edge stall and the consequent loss of lift. Dynamic overshoot was observed in both the lift loss and recovery phases.

5) Based on the observations of the wind tunnel test data, a preliminary mathematical model of aircraft wing rock was developed that illustrated the motion-coupled limit cycle mechanism. Since the limit cycle defining the energy input to the aircraft was dependent on a number of flight condition parameters, no uniqueness condition could be established to define and predict wing rock. Nevertheless, it was known that wing rock was directly related to the lift loss (ramp) of the C_p vs α curve covering the fluctuating-pressure-active region of the wing. Additional acquisition and processing of controlled test data could further refine and quantify the preliminary mathematical model of aircraft wing rock described in this paper.

Acknowledgments

The work reported in this paper was based on the test results obtained under NASA Ames Research Center Contract NAS2-8734, "F-5A Wind Tunnel Buffet Investigation." The writers wish to acknowledge the support and assistance of Charles Coe, Donald Buell, and Denis Riddle of NASA Ames. Among Northrop personnel, the participation and assistance of Dr. Wilford Wong, Brent Bennett, Mel Sanders and Warren Tribble are also acknowledged.

References

[1] Hwang, C., and Pi, W.S., "Northrop F-5A Aircraft Transonic Buffet Pressure Data Acquisition and Response Analysis," *Journal of Aircraft*, Vol. 12, Sept. 1975, pp. 714-720.

[2] Hwang, C., and Pi, W.S., "Investigation of Northrop F-5A Wing Buffet Intensity in Transonic Flight," NASA CR-2484, Nov. 1974.

[3] Ericsson, L.E. and Reding, J.P., "Dynamic Stall Analysis in Light of Recent Numerical and Experimental Results," *Journal of Aircraft*, Vol. 13, April 1976, pp. 248-255.

[4] Halfman, R.L., Johnson, H.C., and Haley, S.M., "Evaluation of High Angle of Attack Aerodynamic Derivative Data and Stall Prediction Techniques," NACA TN-2533, Nov. 1951.

[5] Liiva, J., "Unsteady Aerodynamic and Stall Effects on Helicopter Rotor Blade Airfoil Sections," *Journal of Aircraft*, Vol. 6, Jan. 1969, pp. 46-51.

[6] Eckhaus, W., "A Theory of Transonic Alieron Buzz, Neglecting Viscous Effects," *Journal of the Aerospace Sciences*, Vol. 29, June 1962, pp. 712-718.